Distinct magnetic ground states in Shastry-Sutherland lattice materials: $Pr_2Be_2GeO_7$ versus $Nd_2Be_2GeO_7$

Andi Liu,[1,2] Fangyuan Song,[1] Yaotao Cao,[2] Han Ge,[3] Huanpeng Bu,[3] Jin Zhou,[1] Yuqi Qin,[1] Qingyuan Zeng,[1] Jingxin Li,[4] Langsheng Ling,[4] Wei Tong,[4] Jieming Sheng,[3,5] Ming Yang,[1] Liusuo Wu,[3,*] Hanjie Guo,[2,†] and Zhaoming Tian[1,‡]

[1]*Wuhan National High Magnetic Field Center and School of Physics, Huazhong University of Science and Technology, Wuhan, Hubei 430074, China*

[2]*Songshan Lake Materials Laboratory, Dongguan, Guangdong 523808, China*

[3]*Department of Physics, Southern University of Science and Technology, Shenzhen 518055, China*

[4]*Anhui Key Laboratory of Low-Energy Quantum Materials and Devices, High Magnetic Field Laboratory, HFIPS, Chinese Academy of Sciences, Hefei, Anhui 230031, China*

[5]*School of Physical Sciences, Great Bay University, Dongguan 523000, China*

(Received 4 February 2024; revised 17 April 2024; accepted 22 April 2024; published 7 May 2024)

The rare-earth (RE) based Shastry-Sutherland lattice (SSL) materials have attracted recent attention for exploring the exotic magnetic phases of $4f$ electrons. Here, we present a comparative study on low-temperature magnetization and specific-heat results of two tetragonal structure compounds $RE_2Be_2GeO_7$ (RE = Pr, Nd), where the non-Kramers Pr^{3+} ($J = 4$) ions and Kramers Nd^{3+} ($J = 9/2$) ions are located on the SSL geometry with "AA"-type stacking fashion along the [001] axis. Temperature-dependent magnetic susceptibility and isothermal field-dependent magnetization $M(B)$ measurements reveal that these two compounds share a similar Ising-like magnetic anisotropy with easy magnetization along the [001] axis and additional fourfold symmetry within the *ab* plane. For their magnetic ground states, $Nd_2Be_2GeO_7$ exhibits the coexistence of short-range spin correlation and long-range magnetic order with $T_N = 0.26$ K in zero magnetic field, while $Pr_2Be_2GeO_7$ does not show any signature of long-range magnetic ordering at temperatures as low as 0.08 K. The ac susceptibility and specific-heat analysis of $Pr_2Be_2GeO_7$ reveal a dynamic spin-freezing behavior below ~0.22 K similar to that observed in Pr-based pyrochlore spin-ice systems.

DOI: 10.1103/PhysRevB.109.184413

I. INTRODUCTION

Geometrically frustrated magnets provide a fertile playground for exploring novel quantum states of matter and emergent magnetic phenomena due to the large quantum spin fluctuation and competing interaction on the magnetic ground state. The two-dimensional (2D) magnets with different kinds of frustrated spin-lattice motifs are of particular interest since quantum spin fluctuations can be enhanced by the low dimensionality [1–4]. Among them, the Shastry-Sutherland lattice (SSL) magnets initially realized in $SrCu_2(BO_3)_2$ represent one type of 2D frustrated spin systems and have gained special attention for exploring the exotic magnetic states and unconventional quantum criticalities [5–9]. For such a system, its physical behaviors can be understood based on the Shastry-Sutherland (SS) model consisting of an orthogonal arrangement of spin dimers on the 2D plane as illustrated in Fig. 1(b). The competition between nearest-neighbor (NN) intradimer (J') and next-nearest-neighbor interdimer exchange interactions (J) can lead to magnetic frustration, and by changing the ratio of two exchange interactions $\delta = J/J'$, diverse magnetic ground states appear in the phase diagram, such as the spin-dimer singlet, plaquette order, and long-range magnetic order segregated by a critical ratio δ of 0.675 and 0.765 [6–11], respectively. The magnetic ground state of $SrCu_2(BO_3)_2$ is a gapped dimer singlet state [6,8], and it can be tuned by nonthermal control parameters owing to the nearness of $\delta \sim 0.63$ to the quantum critical point between the dimer singlet and plaquette state. Indeed, the crystallization of different spin superlattices in $SrCu_2(BO_3)_2$ have been identified under extreme physical conditions such as high pressure and high magnetic field [8–13].

The rare-earth (RE) based SSL materials have also attracted much research interest in recent years. Compared to the $3d$ transition-metal (TM) compounds, the strong spin-orbit coupling and crystalline electric field (CEF) effect for RE ions can bring highly anisotropic magnetic exchange interactions, which render the RE-based SSL compounds promising to realize the novel magnetic phases beyond the $3d$ TM-based counterparts. Moreover, the much smaller exchange interactions between the RE^{3+} local moments allow an easy tunability of spin states through the external field accessible in the laboratory; this is distinct from the $SrCu_2(BO_3)_2$ where a full polarization of the Cu^{2+} moments requires an ultrahigh magnetic field beyond 140 T [14,15]. So far, most studies on RE-based SSL materials are limited to the intermetallic compounds including the tetraborides REB_4 [16–18],

*Corresponding author: wuls@sustech.edu.cn
†Corresponding author: hjguo@sslab.org.cn
‡Corresponding author: tianzhaoming@hust.edu.cn

 ©2024 American Physical Society

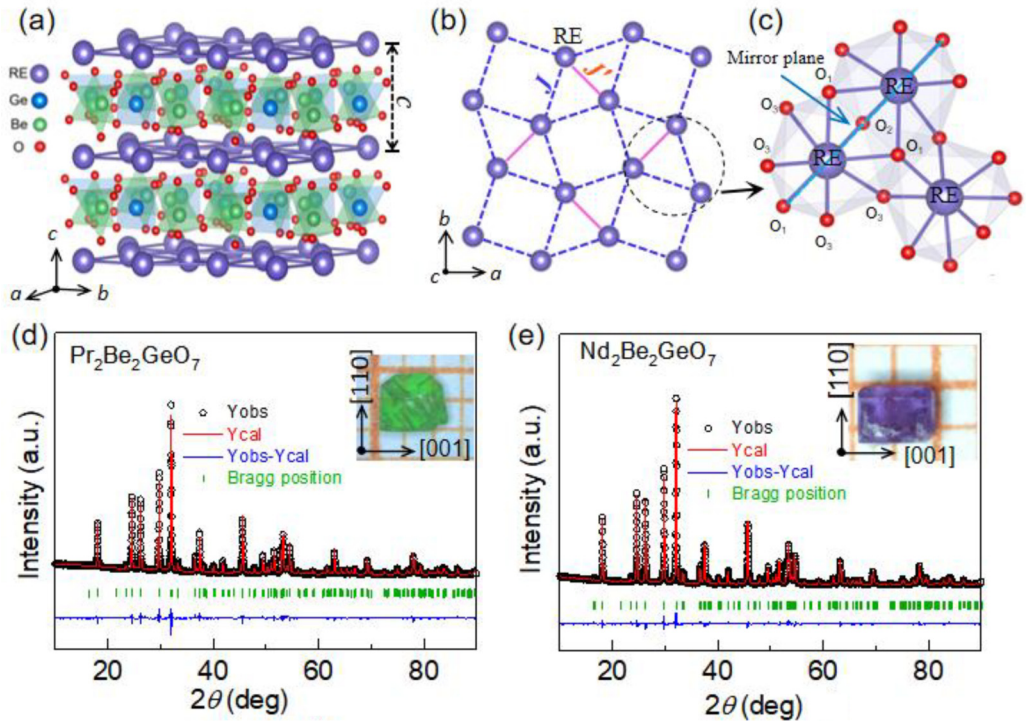

FIG. 1. (a) The crystal structure of $RE_2Be_2GeO_7$ (RE = Pr, Nd). The violet, green, and blue balls denote the RE, Be, and Ge atoms, respectively. The SS lattice layers of RE^{3+} ions are separated by the nonmagnetic polyhedrons along the c axis. (b) The SS lattice networks of RE^{3+} ions within the ab plane; the solid pink and dotted purple lines represent triangle and square bonds of the SS lattice. (c), (d) The experimental (black cycles) and refined (red line) powder XRD patterns of crashed $Pr_2Be_2GeO_7$ and $Nd_2Be_2GeO_7$ single crystals; the blue lines show the difference between the observed and the calculated patterns. The insets of (c) and (d) respectively show the images of as-grown $Pr_2Be_2GeO_7$ and $Nd_2Be_2GeO_7$ single crystals.

RE_2Pt_2Pb [19,20], RE_2T_2In (T = transition metal) [21,22], etc. In such systems, due to the coexistence of localized and itinerant spins, the Ruderman-Kittel-Kasuya-Yosida interactions and Kondo effect have to be considered, complicating the underlying physics of exotic magnetic behaviors. By contrast, the insulating oxides with SSL geometry provide a simple case to unveil the intrinsic SSL physics of localized $4f$ electrons without the influence of conductive electrons. However, only a few compounds have been investigated so far. Among the limited materials, the family of RE_2BaTCh_5 (T = transition metal, Ch = O, S) compounds and its derivatives are one system relatively well characterized [23–25]. The family members Nd_2BaZnO_5 and Nd_2BaPtO_5 are revealed to order antiferromagnetically with Néel temperature T_N = 1.65 K and T_N = 1.9 K [25,26], respectively. In Nd_2BaZnS_5, the exotic spin-dimer liquid state is observed by applying a moderate magnetic field within the SSL plane [27,28]. To further explore the novel magnetic states of RE-based SSL systems, the materials with different stacking sequences of neighboring SSL layers will possibly provide a new route since the way of stacking magnetic layers in frustrated magnets also plays an important role in tuning magnetic frustration and producing different exotic magnetic states [29,30]. Thus, the experimental studies on RE-based SSL magnets with different stacking sequences of SSL layers are essential to enrich the novel magnetic phenomena.

Compared to the AB-type stacking SSL layers in the $RE_2BaZnCh_5$ (Ch = S, O) family, the melilite structure $RE_2Be_2GeO_7$(RE = Pr − Yb) compounds have recently been recognized as the SSL magnets with "AA"-type stacking sequences along the c axis [31], as illustrated in Figs. 1(a) and 1(b), providing another candidate to study the insulating SSL physics. Considering that the Pr^{3+} ($4f^2$, J = 4) ion is a non-Kramers ion with integer spin and the Nd^{3+} ion ($4f^3$, J = 9/2) is a Kramers ion with half-integer spin, these two family members $Pr_2Be_2GeO_7$ and $Nd_2Be_2GeO_7$ allow a comparative study on integer (Pr^{3+}) and half-integer (Nd^{3+}) spins located on the SSL planes. Herein, through the systematic measurements of low-temperature magnetic susceptibility and specific heat down to 50 mK, we investigate the magnetic ground states and anisotropic magnetic behaviors of $RE_2Be_2GeO_7$ (RE = Pr, Nd) single crystals. Both compounds exhibit Ising-like anisotropy with a magnetic easy axis perpendicular to the SSL plane, distinct from the $Nd_2BaZnCh_5$ compounds with magnetic moments lying within the SSL plane. The $Nd_2Be_2GeO_7$ shows the coexistence of short-range and long-range magnetic order behaviors with $T_N \sim 0.26$ K, while $Pr_2Be_2GeO_7$ shows no signature of long-range magnetic ordering down to 0.08 K but exhibits a dynamical spin-freezing behavior below ∼0.22 K.

II. EXPERIMENTAL DETAILS

Single crystals of $RE_2Be_2GeO_7$ (RE = Pr, Nd) were grown via the high-temperature flux method, similar to the previous report [32]. High-quality RE_2O_3 (RE = Pr and Nd;

TABLE I. Crystal data and structure refinement information for $Pr_2Be_2GeO_7$ and $Nd_2Be_2GeO_7$ single crystals.

Formula	$Pr_2Be_2GeO_7$	$Nd_2Be_2GeO_7$
Formula weight	484.43	491.09
Crystal system	Tetragonal	Tetragonal
Space group; Z	$P\text{-}42_1m$; 2	$P\text{-}42_1m$; 2
a, b(Å)	7.5933(2)	7.5726(11)
c (Å)	4.9111(2)	4.8894(7)
α, β (°)	90	90
γ (deg)	90	90
V (Å^3)	283.165(19)	280.38(9)
Density (cal) (g/cm^3)	5.682	5.817
λ (Å)	1.34139	0.71073
θ (deg)	7.176–56.954	4.168–32.003
μ (mm^{-1})	83.026	23.550
T (K)	100	296
F (000)	428	432
Crystal size (mm^3)	0.06 × 0.03 × 0.02	0.08 × 0.06 × 0.04
Final R indices	$R_1 = 0.0426$	$R_1 = 0.0221$
	$wR_2 = 0.0950$	$wR_2 = 0.0537$
R indices (all data)	$R_1 = 0.0470$	$R_1 = 0.0228$
	$wR_2 = 0.0967$	$wR_2 = 0.0544$
Largest diff. peak and hole (e Å^{-3})	2.541 and −1.477	1.472 and −1.008
Goodness of fit on F^2	0.977	1.100

99.99%), BeO (99.9%), and GeO_2 (99.99%) were employed as starting materials and PbO (99.9%) was used as the flux. The rare materials of RE_2O_3, BeO, GeO_2, and PbO with molar ratios of 1:2:1:10 were thoroughly ground and placed in a 40 ml platinum crucible, and then the crucibles were heated at 1423 K for 24 h in a box furnace to ensure the homogeneous melting reaction. After that, the temperature was cooled slowly to 1073 K at a rate of 2 K/h. After furnace cooled to the ambient temperature, the crystals with millimeter level can be recovered from the flux by boiling in water and filtering. Two photos of as-grown $Pr_2Be_2GeO_7$ and $Nd_2Be_2GeO_7$ single crystals are shown in the inset of Figs. 1(d) and 1(e), respectively. The crystal structure of single crystals was checked by a Bruker x-ray diffraction (XRD) equipped with graphite-monochromated Mo $K\alpha$ radiation ($\lambda = 0.71073$ Å). The refinements were performed using the SHELXL least-squares refinement package with the OLEX2 program [33]. The obtained crystal data from the structure refinements are provided in Table I and Table S1 in the Supplemental Material [34]. Also, the crystal structure and phase purity were examined by the powder x-ray diffraction (PXRD; Smartlab) for the crushed single crystals using Cu $K\alpha$ radiation ($\lambda = 1.5418$ Å) in the range of $2\theta = 10^\circ - 80^\circ$. Rietveld refinements on the powder XRD patterns were performed using the FULLPROF program [35]. The CEF calculations based on the point-charge model were performed using the MCPHASE software [36].

Magnetic properties were measured using a Quantum Design magnetic property measurement system and a physical property measurement system (PPMS) equipped with a vibrating sample magnetometer option. Temperature-dependent magnetic susceptibilities and isothermal magnetization measurements were carried out between 2 and 300 K along different typical crystallographic axes. The ac magnetic susceptibility with temperature down to 50 mK were recorded under a driven field of 1–3 Oe in amplitude over a frequency range of $\sim 15 \leqslant f \leqslant\sim 10000$ Hz in a PPMSequipped with a dilution refrigerator. The specific-heat measurements were carried out at different applied fields and temperatures down to 80 mK in a PPMS using the heat-capacity option equipped with a dilution refrigeration system. The zero-field specific heat of a $La_2Be_2GeO_7$ single crystal was also measured down to 2 K and it is extrapolated to lower temperatures from an empirical fit to a T^3 power law, which is used as the nonmagnetic reference of specific heat. The X-band (9.4 GHz) electron spin resonance (ESR) measurements were carried out using a Bruker spectrometer at the High Magnetic Field Laboratory of the Chinese Academy of Science. The pulsed field magnetizations up to 50 T were measured by the induction method at Wuhan National High Magnetic Field Centre (WHMFC) with a calibration by the dc magnetization data.

III. RESULTS AND DISCUSSIONS

A. Crystal structure and crystalline electric field

The experimental and refined PXRD patterns on the crushed $Pr_2Be_2GeO_7$ and $Nd_2Be_2GeO_7$ single crystals are shown in Figs. 1(d) and 1(e), respectively. The structure analysis reveals that both compounds are crystallized into the tetragonal structure with noncentrosymmetric space group $P\bar{4}2_1m$ (No. 113), and the obtained lattice parameters and atomic coordinates are in accordance with the reported ones of polycrystals [30]. The detailed crystal data and selected bond distances are summarized in Table I and Table S1. From that, the refined lattice constants are $a = b = 7.5933(2)$ Å and $c = 4.9111$ Å for $Pr_2Be_2GeO_7$ and $a = b = 7.5726$ Å and

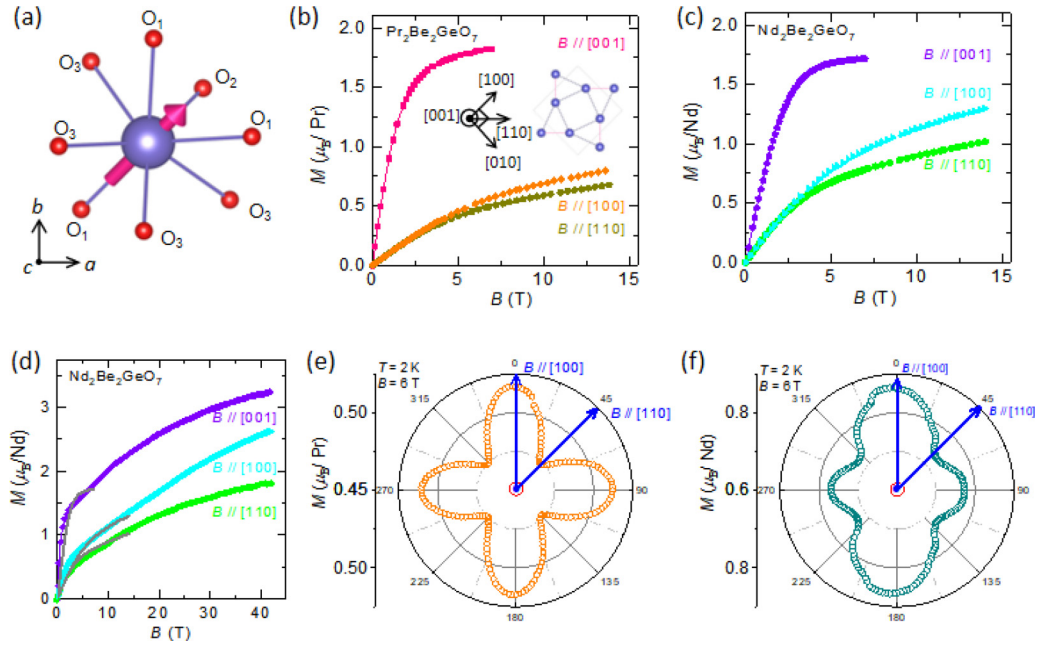

FIG. 2. (a) Local coordination of RE^{3+} in the REO_8 environments. (b), (c) The isothermal magnetization $M(B)$ curves of $Pr_2Be_2GeO_7$ and $Nd_2Be_2GeO_7$ single crystals along different axes. The inset of (a) shows the definitions of three axes with respect to the SS lattice. (d) Field-dependent magnetization of $Nd_2Be_2GeO_7$ single crystals up to 42 T. (e), (f) Angle-dependent magnetization under field of 6 T rotated within the *ab* plane of $Pr_2Be_2GeO_7$ and $Nd_2Be_2GeO_7$, respectively.

$c = 4.8894(7)$ Å for $Nd_2Be_2GeO_7$, respectively. The unit cell consists of the distorted REO_8 dodecahedra, BeO_4 tetrahedra, and GeO_4 tetrahedra. As depicted in Figs. 1(a) and 1(b), magnetic RE ions are arranged on the SSL motif within the *ab* plane and stacked in the AA-type fashion along the *c* axis, and the magnetic SSL layers are well separated by the nonmagnetic $[GeBe_2O_7]^{6-}$ polyhedrons with interlayer's spacing $r^{\text{inter}} = c$, yielding a quasi-two-dimensional (quasi-2D) structure.

Taking $Nd_2Be_2GeO_7$ as a representative, within the SSL plane, the adjacent NdO_8 polyhedron is connected by the face-sharing and edge-sharing fashions for neighboring Nd-Nd ions with the nearest-neighbor (intradimer) bond distance $r_1^{ab} = 3.4302(7)$ Å and next-nearest-neighbor (interdimer) bond separation $r_2^{ab} = 4.0235(7)$ Å, respectively. For the former, the nearest-neighboring Nd^{3+} ions are bridged through three Nd-O-Nd pathways, while for the latter they are connected by two Nd-O-Nd pathways. As illustrated in Figs. 1(b) and 1(c), the direction of the orthogonal spin-dimer chain of the SS lattice is along the [110] axis within the *ab* plane. In terms of the local environments of Nd^{3+} ions, the site symmetry of Nd ions in the distorted NdO_8 polyhedron is a local point group C_s, and the Nd atoms are interchanged by one mirror plane normal to the $[-1\ -1\ 0]$ axis. Compared to the intraplane Nd-O-Nd exchange pathway, the interplane magnetic exchange interactions are via the Nd-O-Ge/B-O-Nd connections with large interlayer's distance $r^{\text{inter}} = 4.8894(7)$ Å, leading to the weaker interplane magnetic exchange interactions. Moreover, no antisite occupations between magnetic Nd^{3+} and nonmagnetic Be^{2+}/Ge^{4+} ions are detected from the structure refinement of single crystals, which is crucial for investigating the intrinsic magnetic behaviors of the SSL of Nd^{3+} moments.

The CEF states are important to understand the magnetic properties of RE-based compounds, thus we performed the CEF calculations based on the point-charge model [37–39]. For the REO_8 polyhedron environment with local symmetry C_s, the ninefold degenerate $J = 4$ ($L = 3$, $S = 1$) multiplet of $Pr^{3+}(^3F_4)$ ions split into nine singlet states, and the tenfold degenerate $J = 9/2$ ($L = 3$, $S = 3/2$) multiplet of $Nd^{3+}(^4I_{9/2})$ ions split into five doublet states. In this local site symmetry, only one mirror plane is preserved without additional rotational symmetry [see Figs. 1(c) and 2(a)]. This constrains the direction of magnetic moments of Pr^{3+}/Nd^{3+} ions within the local (110) mirror plane, and the axis of moments has a canting angle (φ) tilted away from the *c* axis. The canting angle can be determined with the CEF calculation by changing the ground-state wave function with different values of φ, which results in $\varphi = 55.2(55.3)$ for RE = Pr (Nd). The calculated ground-state wave functions are given by $|E0\pm\rangle \approx 1/\sqrt{2}(|-4\rangle \pm |+4\rangle) + \ldots$ for the Pr^{3+} ion and $|E0\pm\rangle = 0.9917|\pm 9/2\rangle \pm 0.0137|\pm 7/2\rangle - 0.1145|\pm 5/2\rangle + \ldots$ for the Nd^{3+} ion, respectively. In $Pr_2Be_2GeO_7$, even the Pr^{3+} is a non-Kramers ion; the CEF calculations reveal a quasidoublet ground state with a small energy gap (~0.039 meV) and a good separation from the next excited CEF level, thus its ground state can be described by a pseudospin-1/2 state. The above calculated wave functions indicate the Ising-like ground state for both compounds with the most contribution from the $|\pm 4\rangle$ for $Pr_2Be_2GeO_7$ and $|\pm 9/2\rangle$ for $Nd_2Be_2GeO_7$. The local environment and spin configuration viewed from the *c* axis of the Pr^{3+}/Nd^{3+} ions are presented in Fig. 2(a), where the Ising axis lies within the (110) plane, denoted by the pink arrow. The orientation of magnetic moments and the related canting angle can be further verified by the magnetization data.

TABLE II. The effective moments ($\mu_{\rm eff}$) and Weiss temperatures ($\theta_{\rm CW}$) of $Pr_2Be_2GeO_7$ and $Nd_2Be_2GeO_7$ single crystals from the Curie-Weiss fitting to the magnetic susceptibility $\chi(T)$ at different temperature regions. The effective moment ($\mu_{\rm fi}$) of free ions is calculated by $g[J(J+1)]^{1/2}$.

		High-T fit (150–300 K)		Low-T fit (4–8 K)		
	Direction	$\theta_{\rm CW}$ (K)	$\mu_{\rm eff}$ (μ_B)	$\theta_{\rm CW}$ (K)	$\mu_{\rm eff}$ (μ_B)	$\mu_{\rm fi}$ (μ_B)
$Pr_2Be_2GeO_7$	B‖[001]	4.04	3.36	−0.33	3.38	3.58
	B‖[100]	−66.7	3.79	−4.89	1.75	
	B‖[110]	−71.4	3.85	−5.13	1.76	
$Nd_2Be_2GeO_7$	B‖[001]	−73.8	3.79	−0.62	2.89	3.62
	B‖[100]	−32.5	3.93	−3.98	2.23	
	B‖[110]	−31.40	3.92	−4.50	2.13	

B. Anisotropic magnetic properties

The isothermal field-dependent magnetization $M(B)$ measurements were carried out on $RE_2Be_2GeO_7$ (RE = Pr, Nd) single crystals at 2 K with B oriented along the [100], [110], and [001] axes. The definition of axes is schematically shown in the inset of Fig. 2(b). As depicted in Figs. 2(b) and 2(c), the $M(B)$ curves of both compounds exhibit a similar Ising-like magnetic anisotropy with easy magnetization along the [001] axis and maximized magnetizations $M_{s,c} \sim 1.85\,\mu_{\rm B}$/Pr and $M_{s,c} \sim 1.75\,\mu_{\rm B}$/Nd, respectively. The obtained magnetizations are $M_{s,110} \sim 0.68\,\mu_{\rm B}$/Pr and $M_{s,110} \sim 1.02\,\mu_{\rm B}$/Nd at 14 T for B‖[110]. Taking that the axis of moments is confined within the (110) plane, the saturated moments (M_s) can be estimated to $M_s \sim 2.3\,\mu_{\rm B}$/Pr and $M_s \sim 2.7\,\mu_{\rm B}$/Nd at low temperatures. Moreover, the ratios of saturated magnetizations ($M_{s,c}/M_{s,110}$)∼2.68 (RE = Pr) and ∼1.71 (RE = Nd) yield $\varphi = 37^\circ$ and $\varphi = 49^\circ$, respectively. Here, the canting angle $\varphi = 49^\circ$ in $Nd_2Be_2GeO_7$ is close to the estimated one by CEF calculations. Along the [100] and [110] axes, the low-field magnetizations exhibit weak magnetic anisotropy for both compounds. In high fields ($B > 3$ T), a more obvious magnetic anisotropy is identified. The ratio of magnetizations ($M_{s,100}/M_{s,110}$) reaches ∼1.19 for RE = Pr and ∼1.30 (1.44) at 14 T (40 T) for RE = Nd [see Figs. 2(c) and 2(d)]. Moreover, angle-dependent magnetizations at 6 T show fourfold symmetry behaviors with maximum value for B ‖ [100] and minimum value for B ‖ [110] [see Figs. 2(d) and 2(e)]. This observed magnetic anisotropy and the ratio of magnetizations $M_{s,100}/M_{s,110}$ are nearly in accordance with the Ising axis lying on the (110) plane for $Nd_2Be_2GeO_7$, which yield the ratio value of $M_{s,100}/M_{s,110} \sim \sqrt{2}$ with the expected spin configurations in high fields as presented in Fig. S2. The slight deviation for $Pr_2Be_2GeO_7$ can be related to the formation of a pair of low-lying CEF singlet states as discussed later. Also, it is to be noted that $Nd_2Be_2GeO_7$ shows the easy magnetization perpendicular to the SSL plane in contrast to the other two SSL compounds $BaNd_2ZnS_5$ and $BaNd_2PtO_5$ [26–28], where the magnetic moments are nearly lying on the SSL plane.

To further evaluate the magnetic anisotropy, temperature-dependent dc magnetic susceptibility $\chi(T)$ under field B = 0.5 T were measured along different axes. In Figs. 3(a) and 3(c), we present the $\chi(T)$ curves with B ‖ [001] and [110] for $Pr_2Be_2GeO_7$ and $Nd_2Be_2GeO_7$, respectively. No magnetic transition or spin freezing are identified down to 1.8 K. In high temperatures, a magnetic crossover occurs at $T_{\rm cross} \sim 240$ K for $Pr_2Be_2GeO_7$ and $T_{\rm cross} \sim 55$ K for $Nd_2Be_2GeO_7$, below which the direction of easy magnetization changes from the ab plane to the c axis, similar to the observation in kagome magnets $RE_3Ga_5SiO_{14}$ (RE = Pr, Nd) [40]. At low temperatures, magnetic susceptibility $\chi(T)$ curves show easy magnetization along the [001] axis, and the anisotropy ratio ($\chi_{[001]}/\chi_{[110]}$) at 2 K is calculated to ∼10.1 (RE = Pr) and ∼3.4 (RE = Nd), respectively. The magnetic susceptibilities are fitted by the Curie-Weiss (CW) law, $\chi = C/(T-\theta_{\rm CW})$, where χ is the susceptibility, C is the Curie constant, and $\theta_{\rm CW}$ is the Curie-Weiss temperature. The resultant magnetic parameters are summarized in Table II. For the high-temperature ($T > 150$ K) CW fits, the effective magnetic moments are close to the values of 3.58 $\mu_{\rm B}$ and 3.62 $\mu_{\rm B}$ of free Pr^{3+} ($4f^3$, $J = 4$) and Nd^{3+} ($4f^3$, $J = 9/2$) ions, but the yielded $\theta_{\rm CW}$ cannot reflect the magnetic interactions between the local moments of RE^{3+} ions due to the thermal population of electrons on different excited CEF levels [41,42]. Thus, the CW fits are also performed at low temperatures (4–8 K), that give $\theta_{{\rm CW},c} = -0.33$ K, $\mu_{{\rm eff},c} = 3.38\,\mu_{\rm B}$/Pr and $\theta_{{\rm CW},a} = -5.13$ K, $\mu_{{\rm eff},\,a} = 1.76\,\mu_{\rm B}$/Pr for $Pr_2Be_2GeO_7$ with B ‖ [001] and B ‖ [110] axes. For $Nd_2Be_2GeO_7$, the fitted values are $\theta_{{\rm CW},c} = -0.62$ K, $\mu_{{\rm eff},c} = 2.89\,\mu_{\rm B}$/Nd, $\theta_{{\rm CW},a} = -4.5$ K,

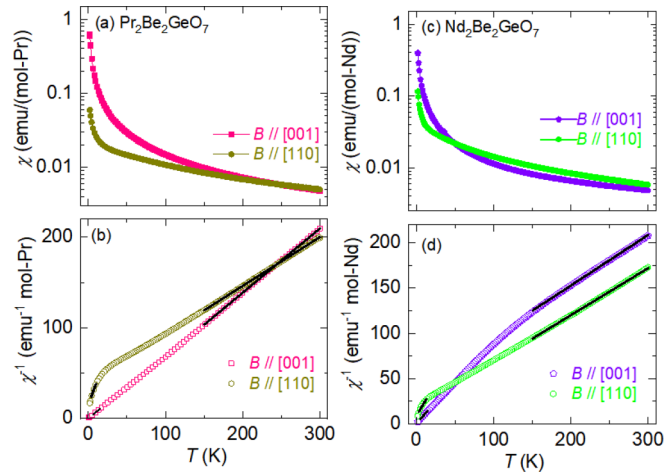

FIG. 3. (a) The dc magnetic susceptibility $\chi(T)$ and (b) inverse magnetic susceptibility $1/\chi(T)$ under a field of 0.5 T of $Pr_2Be_2GeO_7$ single crystal for B along the [001] and [100] axes. The (c) $\chi(T)$ and (d) $1/\chi(T)$ for $Nd_2Be_2GeO_7$ single crystal. The solid black lines in (b) and (d) show the Curie-Weiss fits to experimental data.

TABLE III. The estimated dipolar interactions (D_1^{ab}: nearest-neighbor dipolar interaction; D_2^{ab}: next-nearest-neighbor dipolar interaction; D_c^{inter}: interplane dipolar interaction) and the average magnetic superexchange interaction (J_{ab}: intraplane superexchange interaction; J_c: interplane superexchange interaction) of $RE_2Be_2GeO_7$ (RE = Pr, Nd).

				Dipolar interaction (K)			Superexchange interaction (K)	
	Direction	θ_{CW} (K)	μ_{eff} (μ_{B})	D_1^{ab}	D_2^{ab}	D_c^{inter}	J_{ab}	J_c
$Pr_2Be_2GeO_7$	$B\|\|[001]$	−0.33	3.38	0.173	0.110	0.060		−0.132
	$B\|\|[110]$	−5.13	1.76	0.0467	0.0298	0.0164	−2.05	
$Nd_2Be_2GeO_7$	$B\|\|[001]$	−0.62	2.89	0.348	0.216	0.120		−0.248
	$B\|\|[110]$	−4.5	2.13	0.189	0.117	0.065	−1.80	

and μ_{eff}, $c = 2.13\,\mu_{\text{B}}$/Nd, respectively. The reduced μ_{eff} can be related to the CEF effect where more populations of electrons occupy the low-lying CEF levels at lower temperatures [42]. As summarized in Table II, the fitted θ_{CW} and μ_{eff} for $B \parallel [110]$ are close to those of $B \parallel [100]$, and the negative value of θ_{CW} indicates the primarily antiferromagnetic interactions between the local moments of Pr^{3+}/Nd^{3+} ions within the *ab* plane.

Below, we evaluate the exchange interactions between the RE^{3+} ions in $RE_2Be_2GeO_7$ (RE = Pr, Nd). The strength of dipolar interaction (D) can be estimated by $D = \mu_0\mu_{\text{eff}}^2/[4\pi(R_{\text{NN}})^3]$ [43], where R_{NN} is the space separation between nearest-neighboring RE^{3+} ions and μ_{eff} is the fitted effective moments at low temperatures. The average superexchange interaction (J_{NN}) in the SSL systems can be approximated by the mean-field approximation [1,44], $J_{\text{NN}} = (3k_{\text{B}}\theta_{\text{CW}})/zS_{\text{eff}}(S_{\text{eff}}+1)$, where S_{eff} represents the effective spin quantum number and z is the number of nearest-neighbor spins (here $z = 5$). By taking the low-temperature fitted magnetic parameters θ_{CW}, μ_{eff}, and $S_{\text{eff}} = 1/2$, the estimated D and J_{NN} are summarized in Table III. For both compounds, the intraplane nearest-neighbor dipolar interactions (D_1^{ab}) are around three times larger than the interplane dipolar interactions (D_c^{inter}); moreover, the intraplane superexchange interactions are significantly larger than the interplane ones with $J_{ab}/J_c \sim 15.5$ (RE = Pr) and $J_{ab}/J_c \sim 7.3$ (RE = Nd). Alongside the large interplane space separations, the much larger intraplane magnetic parameters support the quasi-2D nature of these SSL compounds.

C. Specific heat

The specific-heat $C_{\text{p}}(T)$ measurements of $RE_2Be_2GeO_7$ (RE = Pr, Nd) single crystals were performed with temperatures down to ∼0.08 K. As shown in Fig. 4(a), a broad peak maximized at $T_{\text{sr}} \sim 1.6$ K shows up in the zero-field $C_{\text{p}}(T)$ curves characterizing a short-range spin correlation in $Pr_2Be_2GeO_7$, but no λ-like anomaly is detected down to the lowest temperature $T = 0.1$ K, ruling out the formation of long-range magnetic order. By contrast, for $Nd_2Be_2GeO_7$, a λ-shaped peak centered at $T_{\text{N}} = 0.26$ K is observed indicating a long-range magnetic order [see Fig. 4(b)], and it is accompanied by a broad shoulder with maximum at $T_{\text{sr}} \sim 0.5$ K. To estimate the magnetic specific heat $C_{\text{M}}(T)$, the specific heat of nonmagnetic $La_2Be_2GeO_7$ is subtracted and used as the lattice contribution (C_{Latt}). For $Pr_2Be_2GeO_7$, a nuclear specific-heat component (C_{Nuc}) from the hyperfine interaction is also removed as denoted by the dashed lines in a first approximation $C_{\text{Nuc}} \propto 1/T$. The resultant zero-field $C_{\text{M}}(T)$ curves are presented in Figs. 4(c) and 4(d). Despite the low-T anomaly, an additional high-T broad Schottky-like broad peak emerges with maximum at ∼62 K and ∼40 K for $Pr_2Be_2GeO_7$ and $Nd_2Be_2GeO_7$, which is related to the thermal excited occupation of electrons on the excited CEF levels.

The integrated magnetic entropy $S_{\text{M}}(T)$ curves from the zero-field $C_{\text{M}}(T)/T$ data are also presented in Figs. 4(c) and 4(d). For $Pr_2Be_2GeO_7$, the $S_{\text{M}}(T)$ curve flattens out around 15 K, and the release of $S_{\text{M}}(T) \sim 0.89\,R$ ln2 supports the formation of quasidoublet CEF ground states with the magnetic entropy close to R ln2. As T is warmed to 150 K, $S_{\text{M}}(T)$ approaches a saturated value of ∼0.93R ln3. This value indicates the next excited CEF level above the quasidoublet is a singlet state. Considering that this peak comes from the CEF levels of Pr^{3+} ($J = 4$) ions, the experimental data is analyzed

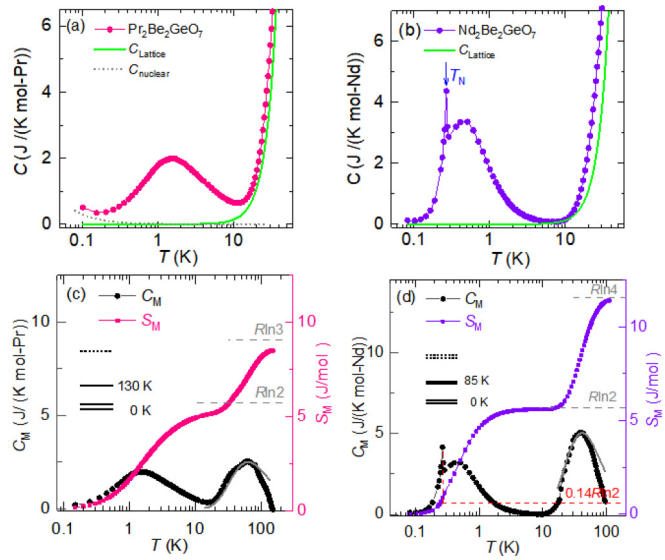

FIG. 4. The zero-field specific-heat $C_{\text{p}}(T)$ results of (a) $Pr_2Be_2GeO_7$ and (b) $Nd_2Be_2GeO_7$ single crystals. The green lines show the specific-heat results of isostructural analog $La_2Be_2GeO_7$; the dashed gray line shows the estimated contribution from the nuclear Schottky effect. (c), (d) The magnetic specific heat $C_{\text{M}}(T)$ and calculated magnetic entropy $S_{\text{M}}(T)$ data of $Pr_2Be_2GeO_7$ and $Nd_2Be_2GeO_7$ crystals; the gray lines show the fitted curves by the two-level Schottky model. The inset shows the low-lying CEF splitting levels.

by the two-level Schottky anomaly model [45,46]

$$C_{\mathrm{Sch}}(T) = nR\frac{g_0}{g_1}\left(\frac{\Delta}{k_{\mathrm{B}}T}\right)^2 \frac{e^{\Delta/k_{\mathrm{B}}T}}{\left[1+\frac{g_0}{g_1}e^{\Delta/k_{\mathrm{B}}T}\right]^2}, \qquad (1)$$

where n is the concentration of Schottky centers, R is the universal gas constant, Δ is the energy gap of the first excited CEF level separated from the quasidoublet ground state in zero field, and g_0/g_1 equals to 2 for the case of the doublet ground state and the first excited CEF singlet state. Then, the CEF splitting energy gap between the ground-state doublet and the first excited singlet is found to be $\Delta \sim 130$ K, as illustrated in the inset of Fig. 4(c). For $Nd_2Be_2GeO_7$, the $S_{\mathrm{mag}}(T)$ curves exhibit a well-defined plateau with the value of R ln2 in temperature intervals of 4–20 K in accordance with the Kramers doublet ground state. At ~100 K, $S_{\mathrm{mag}}(T) \sim R$ ln4 reveals the first excited doublet states, and the corresponding energy gap fitted by the two-level Schottky formula yields $\Delta = 85$ K; the low-lying CEF levels are a schematic in the inset of Fig. 4(d). Further checking the $S_{\mathrm{M}}(T)$ curves of $Nd_2Be_2GeO_7$, we can find only ~14%R ln2 of entropy is reached at $T_{\mathrm{N}} = 0.26$ K; far from the full release of entropy of R ln2 at ~4 K, this implies that the short-range spin correlations develop far above T_{N} possibly driven by magnetic frustration similar to the observation in the kagome-lattice Nd_3BWO_9 systems [47]. Considering the large gap separation between the Kramers doublet ground state and the excited CEF level, $Nd_2Be_2GeO_7$ can be described by an effective $J_{\mathrm{eff}} = 1/22$ moment at low temperatures, and it exhibits the coexistence of a short-range spin correlation and a long-range magnetic ordered state.

The specific-heat measurements at different fields were also carried out for the $B\|[001]$ axis. After subtracting the lattice and nuclear specific-heat contributions (see Fig. S3 for the details), the resultant $C_{\mathrm{M}}(T)$ curves of $Pr_2Be_2GeO_7$ at low-field ($B \leqslant 2$ T) and high-field ($B \geqslant 2$ T) regimes are plotted in Figs. 5(a) and 5(b), respectively. No sharp peak is found in the $C_{\mathrm{M}}(T)$ curves under applied field, revealing the absence of a field-induced magnetic ordered phase. As B is increased, the broad peak shifts to high temperatures and the height of specific heat is initially enhanced and then nearly stays at a constant value of ~3.6 J/(mol-Pr K) for $B \geqslant 4$ T. This suggests that the $C_{\mathrm{M}}(T)$ curves are dominated by the Schottky-like anomaly in high fields ($B \geqslant 4$ T) due to the Zeeman splitting of the quasidoublet ground state of Pr^{3+} ions. Using the two-level Schottky model, the obtained energy gap Δ/k_{B} and n as a function of B are shown in the inset of Fig. 5(c). Moreover, the Δ/k_{B} in the Schottky anomaly can be expressed as $\Delta/k_{\mathrm{B}} = g\mu_{\mathrm{B}}\mu_0 H_{\mathrm{eff}}/k_{\mathrm{B}}$, where $H_{\mathrm{eff}} = \sqrt{H_0^2 + H^2}$ ($H_{\mathrm{eff}} = H_0$ is the crystal field at zero external field and μ_{B} is the Bohr magneton [48–50]). A linear fit yields the zero-field CEF energy gap $\Delta/k_{\mathrm{B}} \sim 2.1$ K, which points out the presence of an intrinsic field in $Pr_2Be_2GeO_7$. This finite zero-field finite gap can arise from the intrinsic splitting between the pair of low-lying CEF ground-state singlets as well as the cooperative magnetism. Moreover, from the value of $\Delta/k_{\mathrm{B}} = 22.8$ K at 10 T, the Landé g factor (g_c) for the $B \parallel [001]$ axis is estimated to be 3.34. This value is close to $g_c \sim 3.1$ evaluated from the ESR spectra [see Fig. S4(a)].

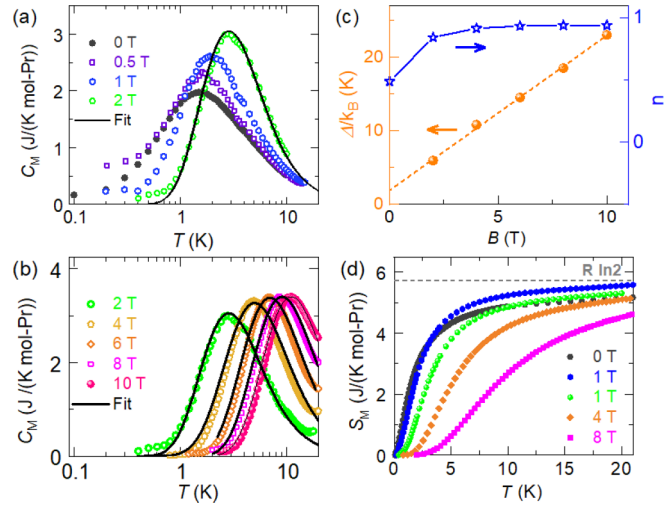

FIG. 5. (a), (b) Magnetic specific-heat $C_{\mathrm{M}}(T)$ curves under different magnetic fields of $Pr_2Be_2GeO_7$ for the $B\|[001]$ axis; the black lines show the fits by the two-level Schottky model. (c) The variation of Δ/k_{B} and the number of free spins versus B. The solid line represents the linear fit of Δ/k_{B}. (d) Magnetic entropy $\Delta S_{\mathrm{M}}(T)$ under different fields of $Pr_2Be_2GeO_7$.

Figure 6(a) shows the $C_{\mathrm{M}}(T)$ curves of $Nd_2Be_2GeO_7$ at low-temperature regions ($0.08\ \mathrm{K} \leqslant T \leqslant 4\ \mathrm{K}$). Under applied field, T_{N} shifts to low temperatures and seems to be suppressed for $B \geqslant 1.5$ T when the system enters into the full polarized state. Meanwhile, the position of a broad peak also moves to higher temperatures, and as increased to $B \geqslant 4$ T, the broad hump in the $C_{\mathrm{M}}(T)$ curves evolves into the Schottky-like

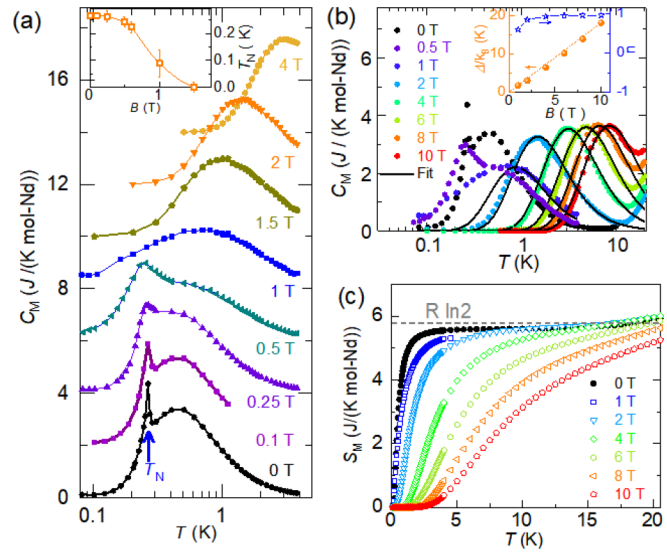

FIG. 6. (a) The magnetic specific heat $C_{\mathrm{M}}(T)$ in different magnetic fields of $Nd_2Be_2GeO_7$ at low temperatures. All data is offset by 2 J/(mol-Nd). The inset shows the variation of T_{N} versus magnetic field. (b) The $C_{\mathrm{M}}(T)$ curves in different magnetic fields. The black lines show the fits by the two-level Schottky model. The inset shows the variation of Δ/k_{B} and n versus B. The solid line represents the linear fit of Δ/k_{B}. (c) Magnetic entropy $\Delta S_{\mathrm{M}}(T)$ in different magnetic fields of $Nd_2Be_2GeO_7$.

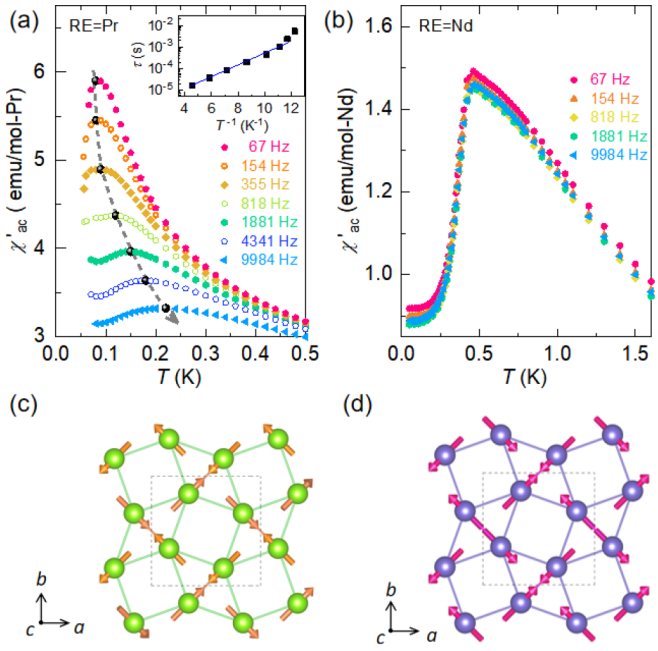

FIG. 7. (a) Temperature dependence of ac susceptibility (χ'_{ac}) measured at various frequencies of $Pr_2Be_2GeO_7$ for the $B\|[001]$ axis. The inset shows the dependence of freezing transition (T_f) on frequency. The solid line denotes the fit to the Arrhenius law. (b) Temperature dependence of ac susceptibility (χ'_{ac}) at different frequencies of $Nd_2Be_2GeO_7$ for the $B\|[001]$ axis. (c),(d) Illustration of the spin configurations at ground state for $Pr_2Be_2GeO_7$ and $Nd_2Be_2GeO_7$.

anomaly behavior, where the $C_M(T)$ data can be well fitted by the two-level model as shown in Fig. 6(b). The obtained Δ/k_B and n versus B are presented in the inset of Fig. 6(b). From the linear fits to the Δ/k_B, zero-field energy gap $\Delta/k_B \sim 0$ K, and $g_c \sim 2.75$ is obtained close to the value of $g_c \sim 2.9$ estimated from the ESR spectra [see Fig. S4(b)]. Also, we can find that the low-field ($B \leqslant 1.5$ T) broad peaks located at 0.5–0.8 K are significantly suppressed for $B \leqslant 1$ T compared to the zero-field ones, and the magnitude of broad peaks at low fields ($B \leqslant 1.5$ T) is much smaller than ~3.6 J/mol K of the value of the Schottky-like anomaly. As shown in Fig. 6(c), the low-field ($B \leqslant 1$ T) $S_M(T)$ approaches R ln2 at $T \sim 4$ K as expected for the Kramers doublet state of Nd^{3+}. As $B \geqslant 2$ T, full release of the magnetic entropy of R ln2 moves to the higher temperatures in accordance with the two-level system.

IV. DISCUSSION AND CONCLUSIONS

From the above experimental results, we can find that the isostructural $Pr_2Be_2GeO_7$ and $Nd_2Be_2GeO_7$ compounds exhibit quite different magnetic ground states. The absence of long-range magnetic order in $Pr_2Be_2GeO_7$ raises the question of whether the magnetic ground state belongs to spin liquid, spin glass, or other magnetic phases with spin freezing. To access the possible spin-freezing behavior in $Pr_2Be_2GeO_7$, the temperature-dependent ac susceptibility was measured down to 50 mK in a dilution refrigerator. Figure 7(a) presents the ac susceptibility data at various frequencies from ~67 to 9984 Hz in zero dc magnetic field. As seen, the real part of susceptibility (χ'_{ac}) shows a broad peak maximized at $T_f \sim 0.083$ K at $f = 67$ Hz, and which shifts to ~0.22 K as increased to $f = 9984$ Hz. Meanwhile, the magnitude of χ'_{ac} is gradually suppressed as frequencies are increased. This frequency dependence of χ'_{ac} indicates a dynamic spin-freezing behavior in $Pr_2Be_2GeO_7$ that is strikingly different from the χ'_{ac} results of $Nd_2Be_2GeO_7$ [see Fig. 7(b)], where the peak position at ~0.43 K almost does not change at different frequencies featuring a long-range magnetic order transition.

Since the presence of a frequency-dependent peak in the ac susceptibility is not the only characteristic of spin glass, we further analyze the spin dynamics behavior of $Pr_2Be_2GeO_7$. The relation of freezing temperature (T_f) versus frequency (f) of χ'_{ac} is analyzed by the Arrhenius law $\tau = \tau_0 \exp(E_b/k_B T_f)$ [51], where $\tau = 1/(2\pi f)$ is the characteristic relaxation time and E_b is the energy barrier. As shown in the inset of Fig. 7(a), the experimental data can be well fitted by the Arrhenius law in frequencies $f > 354$ Hz, which yields the energy barrier $E_b = 0.61$ K and much longer relaxation time $\tau_0 \sim 1.1 \times 10^{-6}$ s. This relaxation time is much longer than that of classical spin glass ($\tau_0 = 10^{-8}$–10^{-9} s) [52–54] but close to the spin-ice systems such as $Pr_2Zr_2O_7$ ($\tau_0 \sim 0.5 \times 10^{-6}$) and $Pr_2Hf_2O_7$ ($\tau_0 \sim 4 \times 10^{-6}$) [55,56]. Additionally, the Mydosh parameter $\phi = \Delta T_f/[T_f \Delta \log(f)] \sim 0.32$, which describes the frequency sensitivity of freezing temperature [51,52,57], is two orders larger than that of canonical spin-glass systems such as AuMn ($\phi \sim 0.0045$) [58] and $YbZnGaO_4$ ($\phi \sim 0.053$) [59] ruling out the spin-glass phase in $Pr_2Be_2GeO_7$. While, this large shift of ϕ has a comparable magnitude with the weak interacting magnetic systems including the quantum spin-ice system such as $Pr_2Zr_2O_7$ ($\emptyset \sim 0.27$) [55] and the superparamagnetic system [60]. Thus, the ac dynamic spin freezing of $Pr_2Be_2GeO_7$ shares some similar features of the Pr-based pyrochlore spin-ice systems, such as the comparable relaxation time, energy barrier, and Mydosh parameter.

For $Nd_2Be_2GeO_7$, the specific-heat results indicate the coexistence of short-range spin correlation and long-range magnetic order, which is different from the single sharp peak observed in the other two SSL $BaNd_2ZnCh_5$ (Ch = O,S) compounds [25,27]. Also, the transition temperature $T_N = 0.26$ K is much lower than the above two compounds with $T_N = 2.9$ K and $T_N = 1.65$ K despite their comparable nearest-neighbor (intradimer) and next-nearest-neighbor (interdimer) distances between Nd^{3+} ions within the SSL plane with $r_1^{ab} \sim 3.46$ Å and $r_2^{ab} \sim 3.51$ Å for $BaNd_2ZnO_5$ and $r_1^{ab} \sim 3.596$ Å and $r_2^{ab} \sim 4.154$ Å for $BaNd_2ZnS_5$. The lower T_N and much less entropy release than R ln2 below T_N [see Fig. 4(d)] support a stronger spin frustration effect in $Nd_2Be_2GeO_7$, and this is in accordance with the large frustration parameter $f = |\theta_{CW}/T_N| \sim 15$ evaluated by the fitted θ_{CW} for the $B\|$ ab plane. Thus, large quantum spin fluctuations should be presented in the ground state of $Nd_2Be_2GeO_7$. An additional difference is that the magnetic structure in the AB-type stacked SSL magnets $BaNd_2ZnCh_5$ is more complex, which consists of two independent Nd sublattices with different propagation vectors [25,28]. Moreover, these two magnetic sublattices respond differently to the applied magnetic field. While, in $Nd_2Be_2GeO_7$, there is a single Nd^{3+} sublattice and the equivalent AA-type stacking structure allows for a simpler system to study the SSL magnetism. In the future, the inelastic

neutron-scattering experiments are required to gain insight into the related exotic spin excitations and emergent magnetic states. As another typical feature of $Nd_2Be_2GeO_7$, the Ising-like Nd^{3+} magnetic moments lie within the (110) plane with a canted angle ∼49 ° away from the c axis. This is quite different from $BaNd_2ZnCh_5$ (Ch = O,S) where the magnetic moments lie on the SSL plane and point perpendicular to the direction of the intradimer Nd-Nd bond confined by the local CEF effect [27,28]. Even for the projected magnetic moments within the SSL plane, the direction of magnetic moments in $Nd_2Be_2GeO_7$ is different and is parallel to the direction of the intradimer Nd-Nd bond. As illustrated in Fig. 7(d), the antiferromagnetic (AFM) magnetic structure should be formed considering the dominant AFM interactions deduced from the low-T susceptibility results of $Nd_2Be_2GeO_7$.

The crystal field splittings in $Pr_2Be_2GeO_7$ and $Nd_2Be_2GeO_7$ are quite different in terms of Pr^{3+} as a non-Kramers ion and Nd^{3+} as a Kramers ion, which can help to explain the distinct ground states in these two systems. Even $Pr_2Be_2GeO_7$ shares a similar Ising-like magnetic anisotropy with $Nd_2Be_2GeO_7$ and its low-T magnetic behaviors can be described by a pseudospin-1/2 moment; but actually there exists small splitting between the two states of the non-Kramers quasidoublet, which can be treated as a transverse field acting on the transverse multipolar components of pseudospin-1/2 moments, as proposed for the rare-earth frustrated magnets containing non-Kramers ions [61–63]. Thus, the magnetic behaviors of $Pr_2Be_2GeO_7$ can be descried by a transverse field Ising model. The intrinsic transverse field can affect the magnetic anisotropy as shown in Fig. 2(b). Moreover, it further competes with the Ising-type interaction and spin-spin interaction. All these competing terms can generate different exotic magnetic phases compared to $Nd_2Be_2GeO_7$ with Kramers doublet ground states. Here, the distinct ground states of $Pr_2Be_2GeO_7$ and $Nd_2Be_2GeO_7$ resemble the observation in the pyrochlore-lattice $Pr_2Zr_2O_7$ and $Nd_2Zr_2O_7$ [55,64,65]; the former exhibits a dynamic spin-freezing behavior and the latter undergoes a long-range magnetic transition. As shown in Fig. 5(d), we can note that the zero-field entropy change $S_M(T) \sim 0.89R$ ln2 at 20 K is less than the expected R ln2 for effective spin 1/2, and the full R ln2 entropy is nearly recovered by applying a small field of 1 T, which results in an entropy difference $\Delta S_M \sim 0.09R$ ln2. This kind of entropy difference is analogous to the three-dimensional (3D) spin-ice materials with the residual entropy ∼0.29R ln2 and the 2D kagome ice with residual entropy ∼0.11R ln2 [55,66], which is ascribed to the formation of 3D and 2D "spin-ice" states, more generally called "emergent charge ordered states" [63,67]. Accordingly, as illustrated in Fig. 7(a), in the case of AFM dimers for the in-plane magnetic moments of Pr^{3+} spins, the "two-in–two-out" spin configurations can be considered to be formed in the rhombus sublattice, where the SSL geometry is actually constructed by the edge co-sharing linkage of a square sublattice and a rhombus sublattice. Namely, in $Pr_2Be_2GeO_7$, the Pr^{3+} spins have an Ising anisotropy axis directed into or out of the rhombus sublattice within the SSL plane and an additional component perpendicular to the SSL plane. In this case, $Pr_2Be_2GeO_7$ offers the platform to realize the possible two-in–two-out spin configuration in the SSL plane as a 2D version of spin ice, and contrastively $Nd_2Be_2GeO_7$ will form the 2D "all-in–all-out" spin configuration. Future neutron-scattering experiments on determining the magnetic structure and magnetic interactions can provide insight into the magnetic ground states and their dynamic properties.

In summary, we have reported the comparative magnetic behaviors on the isostructural $Pr_2Be_2GeO_7$ and $Nd_2Be_2GeO_7$ single crystals with non-Kramers ion Pr^{3+} ($J = 4$) and Kramers ion Nd^{3+} ($J = 9/2$) on the quasi-2D SSL geometry, where the CEF ground states can be respectively described by a non-Kramers quasidoublet with pseudospin-1/2 and a Kramers doublet state with spin-1/2 moments. The $\chi(T)$, $M(B)$ data, and CEF calculations show that both compounds share similar Ising-like magnetic anisotropy with easy magnetization out of the SSL plane and fourfold magnetic symmetry within the SSL plane. For their magnetic ground states, $Pr_2Be_2GeO_7$ shows the absence of long-range magnetic order but a dynamic spin freezing similar to the Pr-based spin-ice system below freezing temperature $T_f \sim 0.22$ K, while $Nd_2Be_2GeO_7$ exhibits the long-range antiferromagnetic phase transition with $T_N \sim 0.26$ K and large spin fluctuations persistent down to low temperatures ($T < T_N$).

ACKNOWLEDGMENTS

This work was supported by the Guangdong Basic and Applied Basic Research Foundation (Grant No. 2022B1515120020) and the Fundamental Research Funds of Guangdong Province (Grant No. 2022A1515010658). Part of the work is supported by National Natural Science Foundation of China (Grants No. 12374146 and No. 11874158). A portion of the measurements was carried out at the Synergetic Extreme Condition User Facility (SECUF) and the Steady High Magnetic Field Facilities. We would like to thank Huifen Ren for her assistance with magnetic measurements and thank the staff of the analysis center of Huazhong University of Science and Technology for their assistance in structural characterizations.

[1] A. P. Ramirez, Strongly geometrically frustrated magnets, Annu. Rev. Mater. Sci. **24**, 453 (1994).

[2] L. Balents, Spin liquids in frustrated magnets, Nature (London) **464**, 199 (2010).

[3] C. Broholm, R. J. Cava, S. A. Kivelson, D. G. Nocera, M. R. Norman, and T. Senthil, Quantum spin liquids, Science **367**, 263 (2020).

[4] A. Vasiliev, O. Volkova, E. Zvereva, and M. Markina, Milestones of low-D quantum magnetism, npj Quantum Mater. **3**, 18 (2018).

[5] B. S. Shastry and B. Sutherland, Exact ground state of a quantum mechanical antiferromagnet, Physica B + C (Amsterdam) **108**, 1069 (1981).

[6] H. Kageyama, K. Yoshimura, R. Stern, N. V. Mushnikov, K. Onizuka, M. Kato, K. Kosuge, C. P. Slichter, T. Goto, and Y. Ueda, Exact dimer ground state and quantized magnetization plateaus in the two-dimensional spin system $SrCu_2(BO_3)_2$, Phys. Rev. Lett. **82**, 3168 (1999).

[7] P. A. McClarty, F. Kruger, T. Guidi, S. F. Parker, K. Refson, A. W. Parker, D. Prabhakaran, and R. Coldea, Topological triplon modes and bound states in a Shastry-Sutherland magnet, Nat. Phys. **13**, 736 (2017).

[8] J. Guo, G. Sun, B. Zhao, L. Wang, W. Hong, V. A. Sidorov, N. Ma, Q. Wu, S. Li, Z. Y. Meng, A. W. Sandvik, and L. Sun, Quantum phases of $SrCu_2(BO_3)_2$ from high-pressure thermodynamics, Phys. Rev. Lett. **124**, 206602 (2020).

[9] Y. Cui, L. Liu, H. Lin, K. Wu, W. Hong, X. Liu, C. Li, Z. Hu, N. Xi, S. Li, R. Yu, A. W. Sandvik, and W. Yu, Proximate deconfined quantum critical point in $SrCu_2(BO_3)_2$, Science **380**, 1179 (2023).

[10] J. L. Jiménez, S. P. G. Crone, E. Fogh, M. E. Zayed, R. Lortz, E. Pomjakushina, K. Conder, A. M. Läuchli, L. Weber, S. Wessel, A. Honecker, B. Normand, Ch. Rüegg, P. Corboz, H. M. Rønnow, and F. Mila, A quantum magnetic analogue to the critical point of water, Nature (London) **592**, 370 (2021).

[11] A. Koga and N. Kawakami, Quantum phase transitions in the Shastry-Sutherland model for $SrCu_2(BO_3)_2$, Phys. Rev. Lett. **84**, 4461 (2000).

[12] M. E. Zayed, Ch. Rüegg, J. Larrea J, A. M. Läuchli, C. Panagopoulos, S. S. Saxena, M. Ellerby, D. F. McMorrow, Th. Strässle, S. Klotz, G. Hamel, R. A. Sadykov, V. Pomjakushin, M. Boehm, M. Jiménez-Ruiz, A. Schneidewind, E. Pomjakushina, M. Stingaciu, K. Conder, and H. M. Rønnow, 4-spin plaquette singlet state in the Shastry–Sutherland compound $SrCu_2(BO_3)_2$, Nat. Phys. **13**, 962 (2017).

[13] Y. Kohama, H. Ishikawa, A. Matsuo, K. Kindo, N. Shannon, and Z. Hiroi, Possible observation of quantum spin-nematic phase in a frustrated magnet, Proc. Natl Acad. Sci. USA **116**, 10686 (2019).

[14] Y. H. Matsuda, N. Abe, S. Takeyama, H. Kageyama, P. Corboz, A. Honecker, S. R. Manmana, G. R. Foltin, K. P. Schmidt, and F. Mila, Magnetization of $SrCu_2(BO_3)_2$ in ultrahigh magnetic fields up to 118 T, Phys. Rev. Lett. **111**, 137204 (2013).

[15] T. Nomura, P. Corboz, A. Miyata, S. Zherlitsyn, Y. Ishii, Y. Kohama, Y. H. Matsuda, A. Ikeda, C. Zhong, H. Kageyama, and F. Mila, Unveiling new quantum phases in the Shastry-Sutherland compound $SrCu_2(BO_3)_2$ up to the saturation magnetic field, Nat. Commun. **14**, 3769 (2023).

[16] J. Etourneau, J. P. Mercurio, A. Berrada, P. Hagenmuller, R. Georges, R. Bourezg, and J. C. Gianduzzo, The magnetic and electrical properties of some rare earth tetraborides, J. Less-Common Met. **67**, 531 (1979).

[17] S. Yoshii, T. Yamamoto, M. Hagiwara, S. Michimura, A. Shigekawa, F. Iga, T. Takabatake, and K. Kindo, Multistep magnetization plateaus in the Shastry-Sutherland system TbB_4, Phys. Rev. Lett. **101**, 087202 (2008).

[18] J. Trinh, S. Mitra, C. Panagopoulos, T. Kong, P. C. Canfield, and A. P. Ramirez, Degeneracy of the 1/8 plateau and antiferromagnetic phases in the Shastry-Sutherland magnet TmB_4, Phys. Rev. Lett. **121**, 167203 (2018).

[19] M. S. Kim, M. C. Bennett, and M. C. Aronson, Yb_2Pt_2Pb: Magnetic frustration in the Shastry-Sutherland lattice, Phys. Rev B **77**, 144425 (2008).

[20] N. Kabeya, S. Takahara, N. Satoh, S. Nakamura, K. Katoh, and A. Ochiai, Antiferromagnetic ground state and heavy-fermion behavior in Ce_2Pt_2Pb, Phys. Rev. B **98**, 035131 (2018).

[21] M. Giovanninia, H. Michor, E. Bauer, G. Hilscher, P. Rogl, and R. Ferro, Structural chemistry, magnetism and thermodynamic properties of R_2Pd_2In, J. Alloy. Compd. **280**, 26 (1998).

[22] G. Sala, S. Mašková, and M. B. Stone, Frustrated ground state in the metallic Ising antiferromagnet Nd_2Ni_2In, Phys. Rev. Mater. **1**, 054404 (2017).

[23] G. F. Goya, R. C. Mercader, M. T. Causa, and M. Tovar, Magnetic properties of *Pnma*-R_2BaZnO_5 oxides (R = Sm, Eu, Dy and Ho), J. Phys.: Condens. Matter. **8**, 8607 (1996).

[24] M. Wakeshima, N. Taira, Y. Hinatsu, A. Tobo, K. Ohoyama, and Y. Yamaguchi, Specific heat and neutron diffraction study on quaternary sulfides $BaNd_2CoS_5$ and $BaNd_2ZnS_5$, J. Solid State Chem. **174**, 159 (2003).

[25] Y. Ishii, G. Sala, M. B. Stone, V. O. Garlea, S. Calder, J. Chen, H. K. Yoshida, S. Fukuoka, J. Yan, C. Dela Cruz, M. H. Du, D. S. Parker, H. Zhao, C. D. Batista, K. Yamaura, and A. D. Christianson, Magnetic properties of the Shastry-Sutherland lattice material $BaNd_2ZnO_5$, Phys. Rev. Mater. **5**, 064418 (2021).

[26] C. M. Pasco, B. K. Rai, M. Frontzek, G. Sala, M. B. Stone, B. C. Chakoumakos, V. O. Garlea, A. D. Christianson, and A. F. May, Anisotropic magnetism of the Shastry-Sutherland lattice material $BaNd_2PtO_5$, Phys. Rev. Mater. **7**, 074407 (2023).

[27] B. R. Billingsley, M. Marshall, Z. Shu, H. Cao, and T. Kong, Single crystal synthesis and magnetic properties of a Shastry-Sutherland lattice compound $BaNd_2ZnS_5$, Phys. Rev. Mater. **6**, 104403 (2022).

[28] M. Marshall, B. R. Billingsley, X. Bai, Q. Ma, T. Kong, and H. Cao, Field-induced partial disorder in a Shastry-Sutherland lattice, Nat. Commun. **14**, 3641 (2023).

[29] J. Q. Liu, X. P. Yao, and G. Chen, Stacking-induced magnetic frustration and spiral spin liquid, Phys. Rev B **106**, L220410 (2022).

[30] X. H. Xu, G. M. Cheng, D. R. Ni, X. Gui, W. W. Xie, N. Yao, and R. J. Cava, Spin disorder in a stacking polytype of a layered magnet, Phys. Rev Mater. **7**, 024407 (2023).

[31] M. Ashtar, Y. M. Bai, L. M. Xu, Z. T. Wan, Z. J. Wei, Y. Liu, M. A. Marwat, and Z. M. Tian, Structure and magnetic properties of melilite-type compounds $RE_2Be_2GeO_7$ (RE = Pr, Nd, Gd−Yb) with rare-earth ions on Shastry-Sutherland lattice, Inorg. Chem. **60**, 3626 (2021).

[32] A. Majchrowski, E. Michalski, and A. Brenier, Growth and spectroscopic characterization of Nd_3BWO_9 single crystal, J. Cryst. Growth **247**, 467 (2003).

[33] G. M. Sheldrick, Crystal structure refinement with *SHELXL*, Acta Crystallogr. Sect. C: Struct. Chem. **71**, 3 (2015).

[34] See Supplemental Material at http://link.aps.org/supplemental/10.1103/PhysRevB.109.184413 for the structure refinement results, the proposed spin configurations, low-T specific heat, and ESR results of $RE_2Be_2GeO_7$ (RE = Pr, Nd) single crystals.

[35] J. Rodríguez-Carvajal, Recent advances in magnetic structure determination by neutron powder diffraction, Phys. B: Condens. Matter **192**, 55 (1993).

[36] M. Rotter, Using McPhase to calculate magnetic phase diagrams of rare earth compounds, J. Magn. Magn. Mater. **272-276**, E481 (2004).

[37] K. W. H. Stevens, Matrix elements and operator equivalents connected with the magnetic properties of rare earth ions, Proc. Phys. Soc. A **65**, 209 (1952).

[38] M. T. Hutchings, Point-charge calculations of energy levels of magnetic ions in crystalline electric fields, Solid State Phys. **16**, 227 (1964).

[39] L. S. Wu, S. E. Nikitin, M. Frontzek, A. I. Kolesnikov, G. Ehlers, M. D. Lumsden, K. A. Shaykhutdinov, E.-J. Guo, A. T. Savici, Z. Gai, A. S. Sefat, and A. Podlesnyak, Magnetic ground state of the Ising-like antiferromagnet $DyScO_3$, Phys. Rev. B **96**, 144407 (2017).

[40] P. Bordet, I. Gelard, K. Marty, A. Ibanez, J. Robert, V. Simonet, B. Canals, R. Ballou, and P. Lejay, Magnetic frustration on a Kagomé lattice in $R_3Ga_5SiO_{14}$ langasites with R = Nd, Pr, J. Phys.: Condens. Matter **18**, 5147 (2006).

[41] J. H. Van Vleck, *The Theory of Electric and Magnetic Susceptibilities* (Oxford University Press, London, 1931).

[42] A. Podlesnyak, S. Rosenkranz, F. Fauth, W. Marti, A. Furrer, A. Mirmelstein, and H. J. Scheel, Crystal-field and magnetic properties of the distorted perovskite $NdGaO_3$, J. Phys.: Condens. Matter **5**, 8973 (1993).

[43] J. S. Gardner, M. J. P. Gingras, and J. E. Greedan, Magnetic pyrochlore oxides, Rev. Mod. Phys. **82**, 53 (2010).

[44] B. C. den Hertog and M. J. P. Gingras, Dipolar interactions and origin of spin ice in Ising pyrochlore magnets, Phys. Rev. Lett. **84**, 3430 (2000).

[45] A. Tari, *The Specific Heat of Matter at Low Temperatures* (Imperial College Press, London, 2003), pp 137−211.

[46] J. Khatua, M. Pregelj, A. Elghandour, Z. Jaglicic, R. Klingeler, A. Zorko, and P. Khuntia, Magnetic properties of the triangular-lattice antiferromagnets $Ba_3RB_9O_{18}$ (R = Yb, Er), Phys. Rev. B **106**, 104408 (2022).

[47] F. Y. Song, H. Ge, A. D. Liu, Y. Q. Qin, Y. Y. Han, L. S. Ling, S. L. Yuan, Z. W. Ouyang, J. M. Sheng, L. S. Wu, and Z. M. Tian, Magnetic-field tuned anisotropic quantum phase transition in the distorted kagome antiferromagnet Nd_3BWO_9, Phys. Rev. B **108**, 214410 (2023).

[48] S. Mahdavifar and A. Akbari, Heat capacity of Schottky type in low-dimensional spin systems, J. Phys.: Condens. Matter **20**, 215213 (2008).

[49] S. Guo, A. Ghasemi, C. L. Broholm, and R. J. Cava, Magnetism on ideal triangular lattices in $NaBaYb(BO_3)_2$, Phys. Rev. Mater. **3**, 094404 (2019).

[50] R. Bag, M. Ennis, C. X. Liu, S. E. Dissanayake, Z. Z. Shi, J. Liu, L. Balents, and S. Haravifard, Realization of quantum dipoles in triangular lattice crystal $Ba_3Yb(BO_3)_3$, Phys. Rev. B **104**, L220403 (2021).

[51] K. Binder and A. P. Young, Spin glasses: Experimental facts, theoretical concepts, and open questions, Rev. Mod. Phys. **58**, 801 (1986).

[52] J. A. Mydosh, *Spin Glasses: An Experimental Introduction* (Taylor & Francis, London, 1993).

[53] E. Lhotel, C. Paulsen, P. D. de Reotier, A. Yaouanc, C. Marin, and S. Vanishri, Low-temperature magnetization in geometrically frustrated $Tb_2Ti_2O_7$, Phys. Rev. B **86**, 020410(R) (2012).

[54] S. X. Huangfu, Z. Guguchia, D. Cheptiakov, X. F. Zhang, H. Luetkens, D. J. Gawryluk, T. Shang, F. O. von Rohr, and A. Schilling, Short-range magnetic interactions and spin-glass behavior in the quasi-two-dimensional nickelate $Pr_4Ni_3O_8$, Phys. Rev B **102**, 054423 (2020).

[55] K. Kimura, S. Nakatsuji, J. J. Wen, C. Broholm, M. B. Stone, E. Nishibori, and H. Sawa, Quantum fluctuations in spin-ice-like $Pr_2Zr_2O_7$, Nat. Commun. **4**, 1934 (2013).

[56] R. Sibille, E. Lhotel, M. C. Hatnean, G. Balakrishnan, B. Fak, N. Gauthier, T. Fennell, and M. Kenzelmann, Candidate quantum spin ice in the pyrochlore $Pr_2Hf_2O_7$, Phys. Rev B **94**, 024436 (2016).

[57] J. Sharma, K. G. Suresh, and A. Alam, Large exchange bias in Mn-Ni-Sn Heusler alloys: Role of cluster spin glass state, Phys. Rev B **107**, 054405 (2023).

[58] A. F. da Silva, Jr., A. S. Martins, and M. F. de Campos, Spin glass transition in AuFe, CuMn, AuMn, AgMn and AuCr systems, J. Magn. Magn. Mater. **479**, 222 (2019).

[59] Z. Ma *et al.*, Spin-glass ground state in a triangular-lattice compound $YbZnGaO_4$, Phys. Rev. Lett. **120**, 087201 (2018).

[60] R. Kumar, P. Yanda, and A. Sundaresan, Cluster-glass behavior in the two-dimensional triangular lattice Ising-spin compound $Li_2Mn_3O_7$, Phys. Rev B **103**, 214427 (2021).

[61] G. Chen, Intrinsic transverse field in frustrated quantum Ising magnets: Physical origin and quantum effects, Phys. Rev. Res. **1**, 033141 (2019).

[62] C. L. Liu, C. J. Huang, and G. Chen, Intrinsic quantum Ising model on a triangular lattice magnet $TmMgGaO_4$, Phys. Rev. Res. **2**, 043013 (2020).

[63] J. G. Rau and M. J. P. Gingras, Frustrated quantum rare-earth pyrochlores, Annu. Rev. Condens. Matter Phys. **10**, 357 (2019).

[64] E. Lhotel, S. Petit, S. Guitteny, O. Florea, M. C. Hatnean, C. Colin, E. Ressouche, M. R. Lees, and G. Balakrishnan, Fluctuations and all-in-all-out ordering in dipole-octupole $Nd_2Zr_2O_7$, Phys. Rev. Lett. **115**, 197202 (2015).

[65] M. Leger, E. Lhotel, M. C. Hatnean, J. Ollivier, A. R. Wildes, S. Raymond, E. Ressouche, G. Balakrishnan, and S. Petit, Spin dynamics and unconventional Coulomb phase in $Nd_2Zr_2O_7$, Phys. Rev. Lett. **126**, 247201 (2021).

[66] G. Möller and R. Moessner, Magnetic multipole analysis of kagome and artificial spin-ice dipolar arrays, Phys. Rev B **80**, 140409(R) (2009).

[67] J. A. M. Paddison, H. S. Ong, J. O. Hamp, P. Mukherjee, X. J. Bai, M. G. Tucker, N. P. Butch, C. Castelnovo, M. Mourigal, and S. E. Dutton, Emergent order in the kagome Ising magnet $Dy_3Mg_2Sb_3O_{14}$, Nat. Commun. **7**, 13842 (2016).